Theoretical investigation of the fully differential cross sections for single ionization of He in collisions with 75-keV protons

L. Gulyás

Institute of Nuclear Research of the Hungarian Academy of Sciences (ATOMKI), H-4001 Debrecen, P.O. Box 51, Hungary

S. Egri

Department of Experimental Physics, University of Debrecen, 18/a Bem tér, H-4026 Debrecen, Hungary

A. Igarashi

Department of Applied Physics, Miyazaki University, Miyazaki 889-2192, Japan

We present a theoretical investigation of the single ionization of He in collisions with H^+ projectile ions at 75-keV impact energy. Using the frameworks of the independent-electron model and the impact parameter picture, fully differential cross sections (FDCS) are evaluated in the continuum distorted-wave with eikonal initial-state approximation (CDW-EIS). Comparisons are made to the recent measurements of Schulz *et al.* [Phys. Rev. A **73**, 062704 (2006)] and Arthanayaka *et al.* [J. Phys. B: At. Mol. Opt. Phys. **49**, 13LT02 (2016)]. Strong influence of the internuclear interaction and effects of target core polarization due to the presence of the projectile ion are observed. Comparing the present results to experimental data and other theoretical predictions, it has been found that the CDW-EIS method qualitatively reproduces structures in the FDCS. Projectile coherence effects are investigated by representing the projectile beam as a Gaussian wave packet. Evidence of interference effects due to projectile-electron and projectile-target core interactions are discussed and the need for further theoretical investigations is proposed.

DOI: 10.1103/PhysRevA.99.032704

I. INTRODUCTION

Single ionization of simple atoms by fast bare ion impact has been the subject of several studies during the last 40 years. Exploring mechanisms leading to the breakup of few-body Coulomb systems represents serious challenges for theoretical investigations as the Schrödinger equation is not analytically solvable for more than two interacting particles. The most complete information on the process of ionization can be obtained by investigating the fully differential cross section (FDCS). Measurement of the FDCS for heavy particle impact is much more demanding than for electron bombardment due to the very small scattering angle and energy loss of the projectile ion. However, in the last few decades, thanks to the development of cold-target recoil-ion momentum spectroscopy (COLTRIMS) [1] the field is enjoying a renewed interest.

Intense efforts to explore the different transition mechanisms in fine details can be observed in recent years [2–5]. It was believed that the relatively simple first Born (B1) approximation would provide adequate description of the ionization mechanisms in the case of very small projectile perturbations (ratio of projectile charge to projectile velocity). Indeed, for 100 MeV/amu C^{6+}-He collisions, the FDCS measured in scattering plane was satisfactorily reproduced by the B1 approximation [6]. However, rather poor agreement was recorded with the measurement taken in the perpendicular plane, and discrepancies remained even for applications of more sophisticated theoretical treatments [7,8]. Initially, the observed discrepancies were attributed to the inadequate treatment of interaction between the heavy colliding partners [9]. While recently, the coherence properties of the projectile and its impact on the processes are in the focus of investigations [5,10,11].

Recently, Schultz *et al.* [12] measured the FDCS for single ionization of Helium by 75-keV proton impact. Their experimental results were compared to data of various distorted wave calculations, including the continuum-distorted wave with eikonal initial state (CDW-EIS) approximation [13–16]. The important role of interaction between the nuclei has been observed, and reasonably accounts of the measured FDCS were reported mostly in the collisions plane. In the perpendicular plane, unexpected structures observed at large transfer momentum values still present a serious challenges for the theoretical treatments. As for the C^{6+}-He system, the incoherent projectile properties were supposed to be responsible for parts of the discrepancies [5].

Projectile coherence and its effects on the interference, due to indistinguishable diffraction of the projectile from different scattering centers, has already been demonstrated for the ionization of H_2 by proton impact [10]. Performing measurements with collimating slits providing projectile beams with transverse coherence lengths that are smaller or larger than the internuclear distance in H_2, it was shown that the cross section depends on the projectile transverse coherence. Recently a different explanation was proposed for

the differences observed between the cross sections taken for different slit distances by Feagin and Hargevas [17]. They interpreted the results of the authors of Ref. [10] as due to the weak collimation property of the incident beam rather than alterations to beam wave packets. However, it should be noted that the numerical result presented for demonstrating the idea of the authors of Ref. [17] was based on incorrect estimation of the divergence for the projectile beam [5,18]. For atomic targets the size of the diffracting object is the typical impact parameter separation between the contributing processes, like first- and higher-order transition mechanisms [5]. This phenomena was justified in the process of transfer ionization in 16 MeV O^{7+}-He collision [19]. However, no interference was found for single ionization, as this process has been found to take place at impact parameters which are larger than the projectile coherence length applied in the study. Interference due to molecular and atomic targets are dubbed as two- and single-center interference [20].

Very recently, Arthanayaka *et al.* [20] investigated the projectile coherence effects for single ionization in the 75-keV H^+-He collision choosing the same kinematic regions as applied in Ref. [12]. Transverse coherence length of the projectile beam was controlled by placing the collimating slit at an appropriate distance from the target. The interference structures observed in ratios of FDCSs taken by coherent and incoherent projectiles were attributed to coherent superposition of different impact parameters leading to the same scattering angle. Therefore, a smaller role for the interference between the first- and higher-order transitions mechanisms was concluded.

In this paper we present a theoretical study of single ionization in a 75-keV H^+-He collision system. The FDCS is evaluated in the CDW-EIS method [21,22], and results are discussed in comparison to the experimental data of Schulz *et al.* [12] and Arthanayaka *et al.* [23] and with available theoretical results. The CDW-EIS model were successfully applied to calculate the total and differential ionization cross sections of emitted electrons even in collisions where the projectile perturbation was larger than 1 [21,24]. The projectile perturbation is 0.58 for the present collision, which value is close to 0.67 referring to the 2MeV/amu C^{6+}-He collision system, where the CDW-EIS model gives a realistic account of the measured FDCS [25]. Our recent study for single ionization of H and H_2 by 75-keV H^+ projectiles could also be mentioned for justification of the CDW-EIS model [26]. Applying independent electron and impact parameter pictures, the one-electron transition amplitudes are evaluated in the CDW-EIS model, where the role of nucleus-nucleus interaction (NN) is taken into account by a phase factor. The importance of including the NN interaction in the treatments was emphasized in previous studies [13–16]. However, in these studies the effects of nonactive electron, the role of the He^+ core, were considered by a Coulomb potentials with effective charge. In the present work, in addition to the Coulomb field, a short-range potential is also introduced for a more realistic account of the core electron. Moreover, the polarization of the target core ion by the incident projectile ion is taken into account by a polarization potential [27–29]. The indication of single-center interference and the characteristic role of target core polarization are observed at small and large momentum transfer values.

The article is organized as follows. In Sec. II we summarize the main points of our theoretical description. In Sec. III the results are discussed. A summarizing discussion is provided in Sec. IV. Atomic units characterized by $\hbar = m_e = e = 4\pi\epsilon_0 = 1$ are used unless otherwise stated.

II. THEORY

The single ionization of He is treated as a one-electron problem, where only one electron is considered as active during the collision time, while the other one remains bound to its initial state. The nonactive electron is taken into account by an effective potential V_{He} that represents the interactions in the $(1s^2)$ ground-state configuration. This potential is obtained on the Hartree-Fock-Slater self-consistent field calculation. The above assumption on the description of the target is the essential point in the application of the independent electron model (IEM), where electrons are considered to evolve independently and it enables to simplify the treatment of a many-electron collision problem to a three-body system [30].

In the following we consider a three body-collision, where a bare projectile ion ionizes a target initially consisting of a bound system of an electron and a core represented by the V_{He} interaction potential. As a further approximation, we apply the impact parameter method, where the projectile having nuclear charge Z_P follows a straight line trajectory $\mathbf{R} = \boldsymbol{\rho} + \mathbf{v}t$, characterized by the constant velocity $\mathbf{v}$ and the impact parameter $\boldsymbol{\rho} \equiv (\rho, \varphi_\rho)$ [31]. The one-electron Hamiltonian has the form

$$h(t) = -\frac{1}{2}\Delta_{\mathbf{r}_T} + V_{He}(|\mathbf{r}_T|) - \frac{Z_P}{|\mathbf{R} - \mathbf{r}_T|}, \qquad (1)$$

where $\mathbf{r}_T$ denotes the position vector of the electron relative to the target nucleus. The single-particle scattering equation

$$\left(h(t) - i\frac{\partial}{\partial t}\Big|_{\mathbf{r}_T} \right)\psi(\mathbf{r}_T, t) = 0 \qquad (2)$$

is solved within the framework of the CDW-EIS approximation, where $\mathbf{r}_T$ and t are considered to be independent coordinates [32]. Details on the applied CDW-EIS method, where unperturbed atomic orbitals in both the incoming and outgoing channels were evaluated numerically on the same V_{He} potential, can be found in our previous papers [21,22,33].

The FDCS differential in energy E_e $(= k_e^2/2)$ and emission angle (θ_e, φ_e) of the emitted electron [$\mathbf{k}_e \equiv (k_e, \theta_e, \varphi_e)$ is the electron momentum] and in the transverse component [$\boldsymbol{\eta} \equiv (\eta, \varphi_\eta)$] of the projectile's momentum transfer $\mathbf{q} = \mathbf{k}_i - \mathbf{k}_f = (\eta\cos\varphi_e; \eta\sin\varphi_e; \Delta E/v)$ is given as

$$\frac{d\sigma}{dE_e\Omega_{k_e}d\boldsymbol{\eta}} = k_e|\mathcal{R}_{i\mathbf{k}}(\boldsymbol{\eta})|^2, \qquad (3)$$

where $\Delta E = E_e - \varepsilon_i$, ε_i is the ionization energy of the electron in the initial state, $\mathbf{k}_{i(f)}$ stands for the projectile momentum before (after) the collision, and $\mathcal{R}_{i\mathbf{k}}(\boldsymbol{\eta})$ is the transition matrix.

In Eq. (3) the projectile's momentum transfer and consequently the projectile scattering is defined by the interaction of the projectile with the active electron. However, the scattering of the projectile also depends on its interaction with the target core (NN interaction). We approximate the NN interaction by

the potential

$$V_{NN}(R) = Z_P Z_T / R + V_s(R) + V_{pol}(R), \qquad (4)$$

where

$$V_s(R) = Z_P \langle \psi_{1s} | - 1/|\mathbf{R} - \mathbf{r}| | \psi_{1s} \rangle. \qquad (5)$$

describes the interaction between the projectile and the passive electrons. In Eq. (5) ψ_{1s} is obtained by numerical solution of the Schrödinger equation with the V_{He} potential. Consequently, $V_s(R)$ was also evaluated numerically. It was checked that $\lim_{R\to 0} V_{NN}(R) \to 2Z_P/R$ and $\lim_{R\to\infty} V_{NN}(R) \to Z_P/R$ for $Z_T = 2$.

$V_{pol}(R)$ in Eq. (4) accounts for the (adiabatic) polarization or distortion of the core electron by the incident charged particle [27,34]. Its use is based on the idea that the electric field of the projectile at distance R gives rise to an instantaneous (first-order) distortion of the core-electron orbital, thereby modifying the interaction of those electrons with the projectile. Polarization potentials have been used in many studies up to fairly high projectile energies [28,29,34–37]. No exact form of V_{pol} is available at short distances, therefore, different types of analytical approximations are available, and we consider the following frequently used forms:

$$V_{pol}(R) = -\frac{\alpha Z_P^2}{2(R^2 + d^2)^2}, \qquad (6)$$

where α is the atomic dipole polarizability parameter [35] and d is a "cutoff" parameter whose value is taken as $d = 0.86$ [27] and as $d = 1.67$ [38], and

$$V_{pol}(R) = -\frac{\alpha Z_P^2}{2R^4}[1 - \exp(-(R/r_d)^6)], \qquad (7)$$

with $r_d = 0.355$ [39]. All these polarization potentials have the form $V_{pol}(R) \approx -\alpha/2R^4$ at large distances and differ in the short-range limit due to the "cutoff" parameters or functions which contain parameters estimated on some reasonable assumptions.

Effects of the NN interaction on the scattering process can be investigated by solving the Schrödinger equation for the Hamiltonian (1) with inclusion of the potential (4). However, the solution simplifies remarkably if one considers that (4) depends on R alone and so V_{NN} can be removed from Eq. (1) by a phase transformation. The transition matrix $\mathcal{R}_{i\mathbf{k}}(\boldsymbol{\eta})$ that takes the internuclear interaction into account can then be expressed as [31]

$$\mathcal{R}_{i\mathbf{k}}(\boldsymbol{\eta}) = \frac{1}{2\pi} \int d\boldsymbol{\rho} \, e^{i\boldsymbol{\eta}\boldsymbol{\rho}} a_{i\mathbf{k}}(\boldsymbol{\rho}), \qquad (8)$$

with $a_{i\mathbf{k}}(\boldsymbol{\rho}) = e^{i\delta(\rho)} \mathcal{A}_{i\mathbf{k}}(\boldsymbol{\rho})$, where $\mathcal{A}_{i\mathbf{k}}(\boldsymbol{\rho})$ is the transition amplitude calculated without the internuclear interaction, and the phase due to Eq. (4) is expressed as

$$\delta(\rho) = -\int_{-\infty}^{+\infty} dt V_{NN}(R(t)). \qquad (9)$$

In the following $\delta(\rho)$ is denoted as $\delta_1(\rho)$-$\delta_6(\rho)$ when V_{NN} in Eq. (9) is approximated by $V_{NN} = Z_P Z_T / R$, $V_{NN} = Z_P/R$, $V_{NN} = Z_P Z_T / R + V_s(R)$, V_{NN} of Eq. (4) where V_{pol} is given by Eq. (6) with $d = 0.86$, by Eq. (7) and by Eq. (6) with $d = 1.67$, respectively. Accordingly, the δ_0 denotes a calculation, where the NN interaction is neglected.

The FDCS given by Eq. (3) corresponds to a beam of projectile ions uniformly distributed in space and moving with a definite initial momentum. Such a beam of particles arrives at the target coherently. However, in the last few years there has been an increasing interest on the coherence properties of the projectile ion [5]. Discussion of the collision where the projectile corresponds to a more realistic situation as being well localized in space can be given within the framework of wave packet description. The role of projectile wave packet was investigated by Karlovets *et al.* [40] for studying scattering of a wave packet of fast non relativistic particle off a potential field. Applying the method of the authors of Ref. [40], good agreement with the experimental data for the 75-keV H^+-H_2 collision was reported in [18]. Wave-packet effects for the projectile have been questioned for the case 100-MeV/amu C^{6+}-He collision due to the very low transverse coherence length, and instead wave-packet effects related to the target are suggested for the explanation [8,41].

The general description of the collision with wave packets both for the projectile and for the target is presented in Appendix A, where we present expressions for the effective FDCS designated by the final momenta of (i) ejected electron and scattered projectile, (ii) recoil ion and scattered projectile, and (iii) ejected electron and recoil ion. The initial wave packet for the target (projectile) does not affect the effective FDCS for case (i) (case (iii)). Both initial wave packets affect the effective FDCS for the case (ii). Measurements of Arthanayaka *et al.* [23] for the 75-keV H^+-He and Schulz *et al.* [6] for the 100-MeV/amu C^{6+}-He collision correspond to the cases (ii) and (iii), respectively. Here we give the expression of the FDCS that we used in Sec. III B to discuss results of Ref. [23]. See Sec. 2 of Appendix A for the formulation, however, in the present treatment we include the wave packet only for the projectile, see Sec. III B. The effective FDCS can be expressed as [8,40]

$$\frac{d\sigma'}{d\mathbf{q}_{rec}d\boldsymbol{\eta}} = \int \mathcal{R}_{i\mathbf{k}}^{\star}(\boldsymbol{\eta}')\Phi^{\star}(\mathbf{k}')\mathcal{R}_{i\mathbf{k}}(\boldsymbol{\eta}'')\Phi(\mathbf{k}'')dk_z d\boldsymbol{\eta}'d\boldsymbol{\eta}'', \qquad (10)$$

where $\mathbf{q}_{rec}$ is the momentum of the recoiled target ion, $\Phi(\mathbf{k})$ denotes the wave packet for the incoming projectile and $\mathbf{q}' = \mathbf{k}' - \mathbf{k}_f = -\boldsymbol{\eta}' + \Delta E/v$, $\mathbf{q}'' = \mathbf{k}'' - \mathbf{k}_f = -\boldsymbol{\eta}'' + \Delta E/v$, and $k_z = \sqrt{k^2 - (\boldsymbol{\eta})^2}$. The packet's wave function in the momentum space can be represented as a product of wave functions corresponding to transverse and longitudinal motions $\Phi(\mathbf{k}) = \Phi_\perp(\boldsymbol{\eta})\Phi_{long}(k_z)$ [40]. For the collisions process under consideration, it is reasonable to assume that the longitudinal dispersion of Φ_{long} is much smaller than the scattering length, furthermore, the transition amplitude as a function of k_f changes less rapidly in the region where Φ_{long} is concentrated and so the integral over k can be evaluated separately resulting in $1/\cos(\theta_k)$. θ_k is the opening angle of the wave packet, which also supposing a sharp distribution in the perpendicular direction, can be taken as $\theta_k = 0$.

Finally, the effective FDCS is evaluated as

$$\frac{d\sigma'}{d\mathbf{q}_{rec}d\boldsymbol{\eta}} = \int d\boldsymbol{\eta}' |\Phi_\perp(\boldsymbol{\eta}')|^2 \frac{d\sigma(\boldsymbol{\eta}')}{d\mathbf{q}_{rec}d\boldsymbol{\eta}'}, \qquad (11)$$

where for the present study $|\Phi_\perp(\boldsymbol{\eta})|^2$ is given by

$$|\Phi_\perp(\boldsymbol{\eta})|^2 = \frac{2d_x d_y}{\pi} \exp\left(-2d_x^2 k_x^2 - 2d_y^2 k_y^2\right), \qquad (12)$$

where $\boldsymbol{\eta}' = \boldsymbol{\eta} + \mathbf{k}_\perp$, $\mathbf{k}_\perp = (k_x, k_y)$, and d_x and d_y are parameters for the coherence length (average size) of the wave packet in the x and y directions.

III. RESULTS

In this section we present and discuss results for the 75-keV H^+-He collision at $E_e = 5.4$ eV electron emission energy. Slow electrons are usually ejected in distant collisions between the projectile and the target nucleus where the three-body dipole interaction dominates [24]. The dominant contribution of the $l = 0, 1$ terms in the transition amplitude expanded over spherical harmonics is the characteristic feature of the dipole interaction [21]. The present collision system complies with these requirements, as taking into account only the $l = 0$–2 partial waves in the calculation provides the complete DDCS over the whole angular range, and considering only the $l = 0, 1$ terms gives already 90–95% of the correct DDCS value. Furthermore, the region of ρ over which the transition amplitude is nonnegligible extends up to $\rho = 4$–6. First, we discuss results where coherence properties of the projectile are not considered, that is calculations are performed with a coherent projectile, see Eq. (3). Results considering an incoherent projectile beam are presented and discussed in the second part of the section.

A. Collision with coherent projectile beam

In Figures 1 to 6 we discuss our CDW-EIS results of fully differential cross sections and compare them to measurements and other theoretical data. FDCSs for electrons ejected into the scattering and perpendicular planes are calculated for different transfer momentum values η of 0.13, 0.41, 0.73, and 1.38. The scattering plane is the plane containing both the incident and the scattered momentum vectors of the projectile ion, while the perpendicular plane also includes the momentum vector of the incident projectile, however, its normal vector is fixed by $\boldsymbol{\eta}$. That is, the scattering plane lies in the xz plane, where the x axis is defined by the transverse component of $\mathbf{q} (=\boldsymbol{\eta})$ and the z direction by the initial projectile beam axis, and the perpendicular plane is fixed by the yz plane. Figures 1 and 2 show the present results evaluated without and with the NN interaction, where different approximations have been applied to the internuclear and polarization potentials [see Eqs. (4) to (7) and (9)]. The role of V_{NN} is obvious, it has influences both on the shape and magnitude of the reference FDCS obtained without V_{NN}. Furthermore, discrepancies among results obtained by using different approximations to V_{NN} are also remarkable. Calculations without V_{NN} show the best accounts of the measurements at the lowest η value and overestimate the experimental data with the increase of η. At the same time, considering the magnitude of the FDCS, calculations including V_{NN} give the least acceptable results at $\eta = 0.13$, while their results fall within the range of experiment at large η values. It is also well seen in Figs. 1 and 2 that the FDCSs calculated with different forms of V_{NN} are in

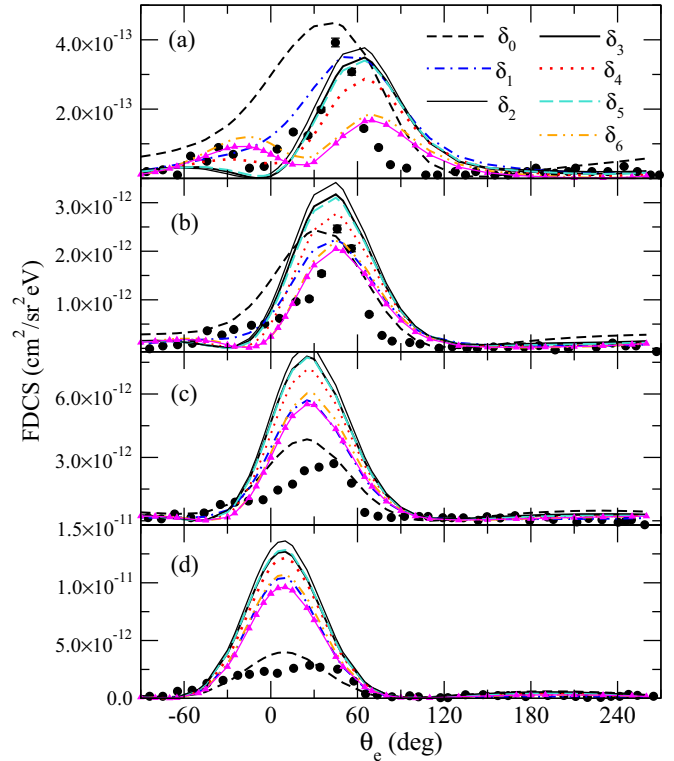
FIG. 1. FDCS for electrons with an energy of 5.4 eV ejected into the scattering plane $[\mathbf{k}_e = (k_e \sin\theta_e, 0, k_e \cos\theta_e), \varphi_e = 0°]$ in 75-keV H^+ + He collisions. The transverse momentum transfers are (from bottom to top) 0.13, 0.41, 0.73, and 1.38. Theories: Present results, dashed black lines represent calculations without NN interaction (phase δ_0); calculations where the NN interaction is represented by internuclear phase δ_i, $i = 1$–6 are denoted as dot dashed blue, thin solid black, heavy solid black, dotted red, long dashed turquoise, and dot dot dashed orange lines. Thin magenta line with triangle up: Present results with NN phase of δ_6 convolved with experimental resolution. Experiment: ● from Ref. [12].

the best agreement in shapes and magnitudes at the smallest η values and discrepancies increase with increasing η.

1. Interference between Pe and NN interactions

The observed variation of the FDCS with η in the different model applications can be explained by the following simple picture: As noted above, the emission of an electron due to its interaction with the projectile (Pe) is favored in the $\rho = [0$–$5]$ region. To identify impact parameter regions that may correspond to the different reactions mechanisms let us consider

$$\widetilde{R}_{i\mathbf{k}}(\boldsymbol{\eta}, \rho_m) = \frac{1}{2\pi} \int_0^{\rho_m} \rho d\rho \int_0^{2\pi} d\varphi_\rho \, e^{i\boldsymbol{\eta}\boldsymbol{\rho}} \, \widetilde{a}_{i\mathbf{k}}(\boldsymbol{\rho}) \qquad (13)$$

and evaluate

$$r_{i\mathbf{k}}(\boldsymbol{\eta}, \rho_m) = \lim_{\Delta\rho_m \to 0} [|\widetilde{R}_{i\mathbf{k}}(\boldsymbol{\eta}, \rho_m + \Delta\rho_m)|^2$$
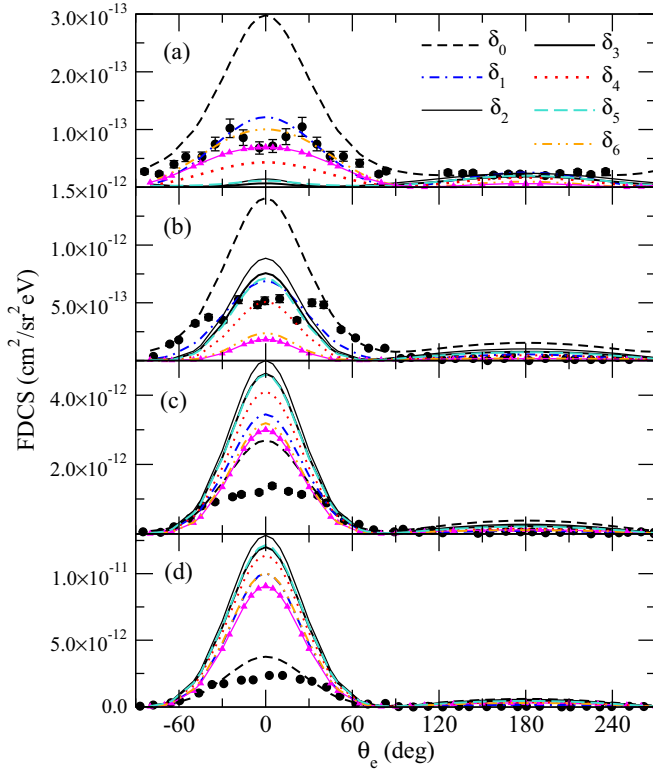$$- |\widetilde{R}_{i\mathbf{k}}(\boldsymbol{\eta}, \rho_m)|^2]/\Delta\rho_m, \qquad (14)$$

FIG. 2. Same as Fig. 1 but for electrons ejected into the perpendicular plane [$\mathbf{k}_e = (0, k_e \sin\theta_e, k_e \cos\theta_e)$, $\varphi_e = 90°$].

where $\widetilde{a}_{i\mathbf{k}}(\boldsymbol{\rho})$ stands for $a_{i\mathbf{k}}(\boldsymbol{\rho})$, $\mathcal{A}_{i\mathbf{k}}(\boldsymbol{\rho})$ or $a_{i\mathbf{k}}(\boldsymbol{\rho}) - \mathcal{A}_{i\mathbf{k}}(\boldsymbol{\rho})$. The last quantity (the difference) is the transition amplitude for the pure NN interaction.

Let us see first the results at $\eta = 0.13$. Taking into account only the Pe interaction [$\widetilde{a}_{i\mathbf{k}}(\boldsymbol{\rho}) = \mathcal{A}_{i\mathbf{k}}(\boldsymbol{\rho})$], a definite peak in $r_{i\mathbf{k}}$, the dominant contribution to the FDCS, can be observed at around $\rho \approx 3$ for all electron emission angles. At the same time, when the NN interaction is also included [$\widetilde{a}_{i\mathbf{k}}(\boldsymbol{\rho}) = a_{i\mathbf{k}}(\boldsymbol{\rho})$] the main contribution is shifted to the $\rho \approx 4$ region. Furthermore, considering the difference [$\widetilde{a}_{i\mathbf{k}}(\boldsymbol{\rho}) = a_{i\mathbf{k}}(\boldsymbol{\rho}) - \mathcal{A}_{i\mathbf{k}}(\boldsymbol{\rho})$] the major increase in the FDCS appears at $\rho \geqslant 5$ values. These observations suggest that significant contributions to the FDCS by the Pe and NN interactions are clearly separated in the impact parameter space. However, the widths of the transition regions for the individual processes are larger than their typical impact parameter separation, and as noted in the full quantal treatment [14], their contributions might interfere constructively or destructively to the FDCS. Pe and NN interfere constructively for the case $\eta = 0.13$, which might explain the extra increase of the FDCS calculated with the inclusion of the NN interaction as compared to the reference FDCS (see the lower panels in Figs. 1 and 2). As noted in the Introduction, this type of interference does not require multiple scattering centers and it is referred to as single-center interference [5,20]. The main contribution of the Pe interaction shifts to lower ρ values with the increase of η, furthermore, the transition zone extends so that the $\rho \geqslant 5$ region presents also the nonnegligible contribution. Therefore, for medium and large η values, the major contribution of the Pe mechanism is not restricted to a limited area, and the

interference with the NN process plays a greater role in the whole ρ space. At around $\eta = 0.7$–1.5 the interference between the two mechanisms is often destructive, and for larger η the determining contribution arrives mostly from the NN mechanism. Special characteristics for the NN interaction become highly decisive in the region of destructive interference as it can be seen in the upper graphs of Figs. 1 and 2. See, for example, FDCSs obtained with δ_1 ($V_{\text{NN}} = Z_P Z_T / R$) and with δ_3 [V_{NN} of Eq. (4) with $V_{\text{pol}} = 0$] phases are comparable at the low η region, however, significant changes can be observed between them at $\eta = 1.38$, especially in the perpendicular plane, where the peak at $\theta_e = 0°$ is almost completely absent in the FDCS in the later calculation.

2. Structures in the FDCS

As the above discussion revealed, the overestimation of the FDCS at low η values can be explained by the constructive interference between the Pe and NN mechanisms. However, at medium and large η values, where the theory shows better results in the absolute scale, structures in the FDCS present the major challenge, see upper graphs in Figs. 1 and 2. Therefore, it is worth considering the FDCS in more detail. Figure 3 presents surface plots of FDCSs for $\theta_e = 45°$ and $90°$. Note that the transition amplitude in the azimuth plane depends on the difference between φ_e and φ_η, therefore, φ_η was fixed to $\varphi_\eta = 0°$ in the calculation. A valley-like structure can be observed in all graphs, which is more prominent for results with NN interaction. This feature of the FDCS is also observable in the B1 calculation, therefore, we resort to this model to explore the origin of the valley structure. The B1 transition probability for the ionization of a H-like atom with effective charge Z_{eff} is given in the Appendix. Two terms A and T depend on the difference $\varphi_\eta - \varphi_e$, see Eq. (B1). The former and the latter are dominant at large and small η regions corresponding to close and distant collisions. T has minimum at $\varphi_\eta - \varphi_e = 180°$ for all η values. While the minimum in A corresponds to the $\mathbf{q}\mathbf{k}_e = q^2 k^2 / (k^2 + Z_{\text{eff}}^2)$ condition, which determines a curve, the position of the valley, in the η-φ_e surface. Note that the value of Z_{eff}, the strength of the interaction between the electron and the target core, has a significant influence on the depth of the valley and so on the significance of a hump at $\varphi_k = 180°$ for medium η values, see Fig. 3.

The FDCS, at $\theta_e = 0°$, does not depend on φ_η and φ_e, therefore, in Fig. 4(a) FDCS versus η is shown. Results obtained with different NN potentials are presented in the figure, which enables to investigate the role of NN in more detail. It can be seen that the various approaches applied to V_{NN} provide FDCS values that are almost the same at small η values. The small η region corresponds to distant collisions between the projectile and target, and only the asymptotic region of V_{NN} is expected to be important. Here we note that test calculations indeed revealed different individual transition amplitudes by the $Z_P Z_T / R$ (δ_1) and Z_P / R (δ_2) interactions, however, their interferences with the contribution of Pe result in similar FDCS values at the small η region. Minimums at $\eta \approx 1.5$ are seen well in results of calculations with δ_2 and δ_3 unlike in the evaluation with δ_1. Dips are also present in calculations with different V_{pol} (see results with
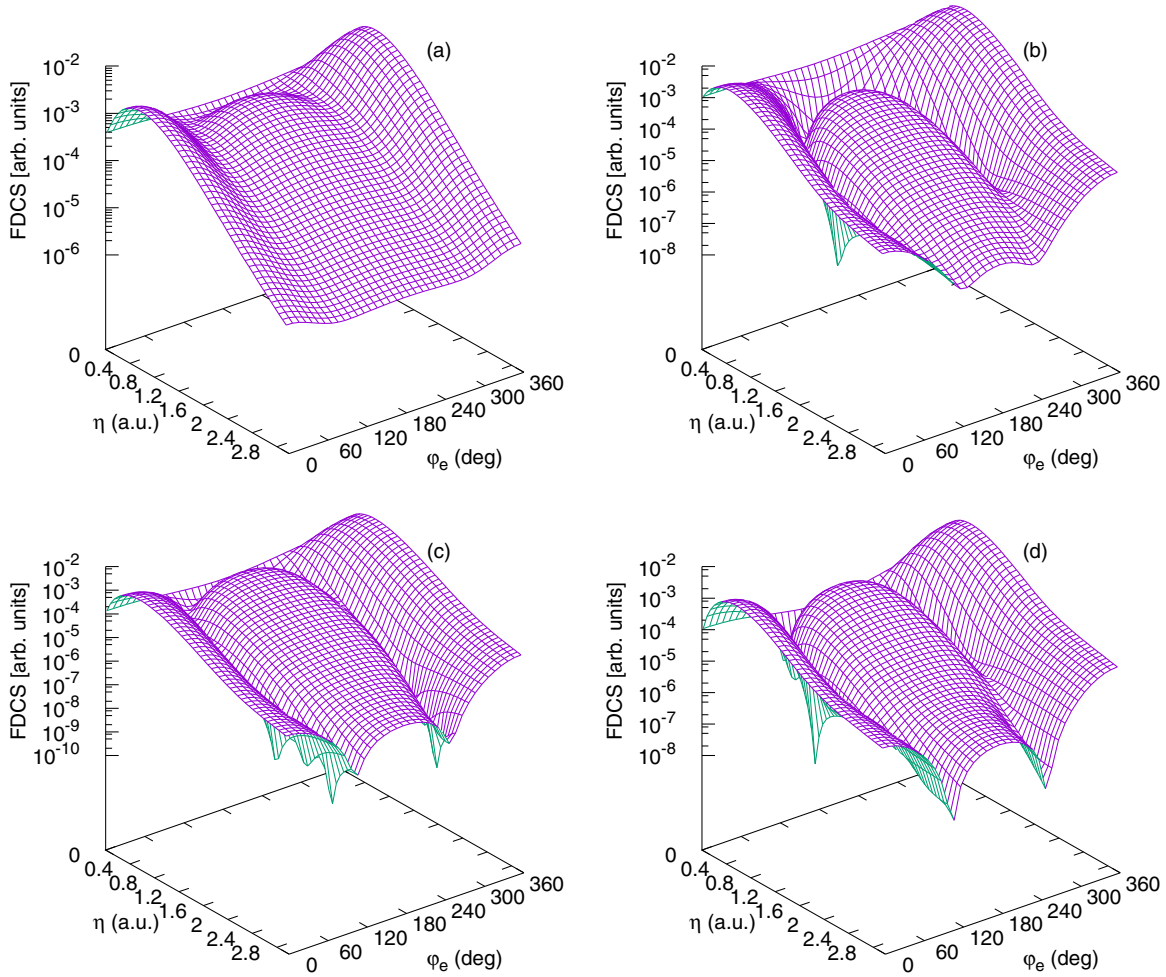
FIG. 3. Surface plot of the FDCS for electrons with an energy of 5.4 eV ejected into $\theta_e = 45°$ (a) and (b) and into $\theta_e = 90°$ (c) and (d) directions in 75-keV p + He collisions in CDW-EIS calculation. Without NN interaction (δ_0) in panel (a); the NN interaction is represented by internuclear phases δ_3 in panels (b) and (c) and δ_4 in panel (d).

δ_4-δ_6), however, their positions shift to lower η values. At large, asymptotic η values the deviations among the different calculations reflect the different character of NN at small distances.

Variation of the FDCS for the different NN phases can be further explored if one considers δ_i as a function impact parameter. Internuclear phases of Eq. (9) for the different approximations are presented in Fig. 4(b). It is seen that at
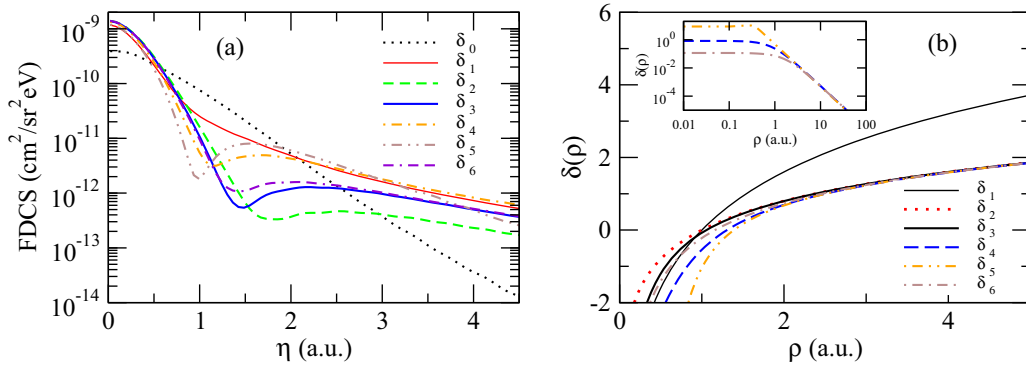

FIG. 4. (a) FDCS for electrons with an energy of 5.4 eV ejected into the forward direction in 75-keV p + He collisions. Present calculations: Without NN interaction dotted line (phase δ_0); calculations where the NN interaction is represented by internuclear phases δ_i are denoted as thin red, dashed green, heavy blue, dot dot dashed orange, dot dashed dashed dot violet, dot dot dashed brown lines, respectively for $i = 1$–6. (b) Internuclear phases δ_i represented by thin solid black, dotted red, heavy solid black, dashed blue, dot dot dashed orange, dot dashed brown lines, respectively, for $i = 1$–6. The inserted figure shows the internuclear phase only for V_{pol} of (6) with $d = 0.86$ a.u. dashed blue, $d = 1.67$ a.u. dot dashed brown, and of Eq. (7) dot dot dashed orange lines.

$\rho \geqslant 2$ all but δ_1 phases reach the same asymptotic limit. At the same time the shapes and positions of the dips are determined by the region of $\rho \leqslant 5$, where considerable differences can be observed among the different approaches seen also in the inserted figure of Fig. 4(b).

As Figures 3 and 4 show, various structures can be observed in the FDCS. Sizes and positions of the minima depend strongly on approximations applied for the NN interaction. The FDCS is the most dominant at $\theta_e \approx 0°$, see Figs. 1 and 2. At $\theta_e = 0°$, the versatility of the FDCS is manifested at $\eta \approx 1.4$ see Fig. 4, which is also reflected in results presented in the upper graphs of Figs. 1 and 2. Note that calculation with $V_{NN} = Z_P Z_T / R$ reveals a dominant single peak in the FDCS at $\theta_e = 0°$. At the same time when the NN interaction is considered by the $V_{NN} = Z_P / R$ potential, only a tiny peak with much lower intensity is produced in the FDCS, see Fig. 2. The best agreement is observed with δ_6, however, the two-peak structure with a minimum at $\theta_e = 0°$ cannot be reproduced in either of our calculations. It can be concluded that the shape and magnitude of the FDCS at $\eta = 1.38$ is highly influenced by the screening role of the passive electron and by the "cutoff" parameter for the polarizbilty of the target core.

3. Comparison to and discussion of other studies

Similar discrepancies in describing the FDCS of the 75-keV H^+-He collision system were already reported in other applications. Overestimation of the FDCS in the small η region, in a CDW-EIS calculation [13], was attributed to the overrated NN interaction (referred to as PI (projectile and residual-target-ion) interaction in Ref. [13]). It was supposed that in reality a combination of active and passive electron clouds might partially screen the target nucleus resulting in a weaker NN interaction. Determining the role of the NN interaction has also been justified in the present CDW-EIS results at small η values, however, the role of NN was found important mostly in regions of the impact parameter where NN already takes its asymptotic value. Therefore, our results suggest that the electron screening has a smaller role, instead interference (by separation or overlap of the relevant impact parameter domains) between the Pe and NN mechanisms plays a much more important role in determining the magnitude of the FDCS. Note that in Ref. [13] the projectile and target core interaction was considered by a pure Coulomb potential with $Z_T = 1$ (like δ_2 in our treatment). Interestingly, the present calculations with a stronger NN interaction ($Z_T = 2$) show smaller FDCS values, see Figs. 1 and 2 with δ_1 and δ_2. In the following the theory of Ref. [13] is referred to as CDW-EISPI distinguishing from the present one that is referred to as CDW-EISNN.

In Ref. [14] the important role of constructive and destructive interferences between Pe and NN in forming the shape of the FDCS was discussed using the three-Coulomb wave (3C) model. Similar conclusions were obtained in Ref. [15] in the modified Coulomb-Born approximation, where NN was also included (MCB-PI). Recently, within the framework of a Born-like approximation a continuum correlated wave (CCW) function has been applied for the final sate [16]. Correlated motion of the ionized electron in the field of heavy particles, considered beyond the three Coulomb (3C) model, and the
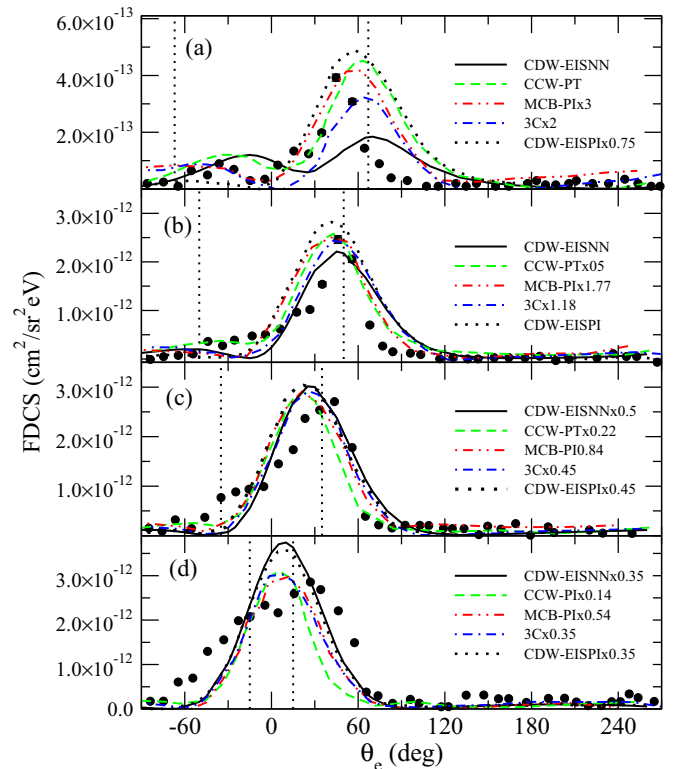

FIG. 5. FDCS for electrons with an energy of 5.4 eV ejected into the scattering plane in 75-keV p + He collisions. θ_e correspond to the electron emission angle defined in the text. The transverse momentum transfers are (from bottom to top) 0.13, 0.41, 0.73, and 1.38. Thin solid black lines: Present results where the NN interaction is represented by internuclear phase δ_6. Dotted lines: CDW-EISPI calculations [13]. Dashed lines: CCW-PT calculations [16]. Dot dashed lines: 3C calculations [14]. Dot dot dashed lines: MCB-PI calculations [15]. Experiment: ● from Ref. [12].

projectile target core (referred to as PT) interaction were identified as having determining roles in forming the shape and magnitude of the FDCS in their CCW-PT theory.

In Figs. 5 and 6 present results with δ_6 are compared to results of other calculations described above. In the comparison we focus on the shape of the FDCS, therefore, to get rid of the different magnitudes of the FDCS from the different calculations, if it was necessary, a given result was multiplied by an appropriate factor shown also in the figures. The best agreement among the theories can be observed at $\eta = 0.13$, where all the models describe reasonably the peaks in measured distributions. At the same time, it has to be noted, the largest discrepancies among the theories in predicting the absolute magnitude of the cross section are observed at this η value. It should also be emphasized that all the theories considerably overestimate the measurement at $\eta = 0.13$. The agreement between theories and experiment is still acceptable for $\eta = 0.41$, and discrepancies become apparent for the $\eta = 0.73$ and 1.38 values. With increasing η the measured peak gets broader and separates into two peaks in the perpendicular plane at $\eta = 1.38$, where the largest variations among predictions of the theories can be observed. The present calculations (see also Fig. 2) do not predict
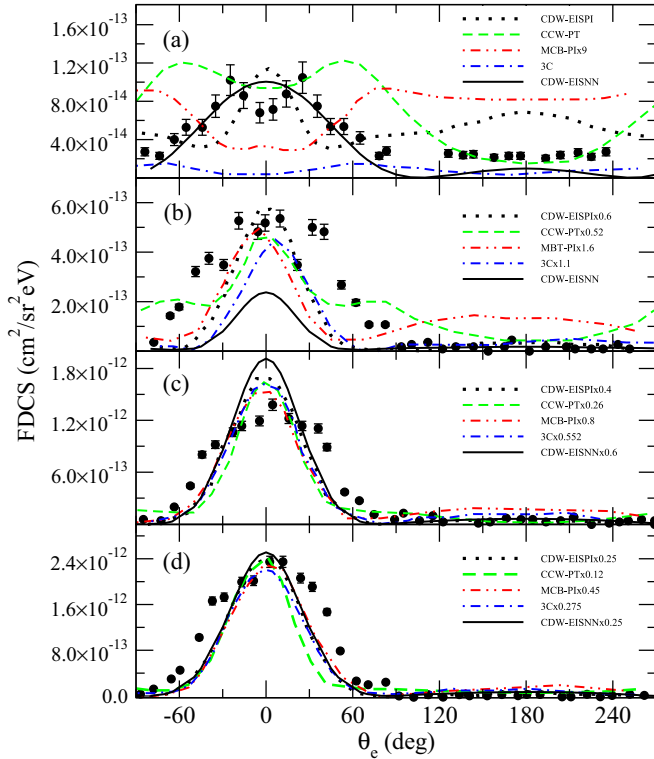
FIG. 6. Same as Fig. 5 but for electrons ejected into the perpendicular plane.

the double peak structure and results with δ_6 gives the best account (also in magnitude) with the measurement. The two-peak structure is qualitatively reproduced by the CCW-PT and MCB-PI calculations, however, the maximum positions predicted at $\theta_e \geqslant \pm 55°$ differ considerably from $\theta_e \approx \pm 30°$ observed in experiment. All these calculations, in agreement with our above statement, report the crucial importance of including projectile target-ion interaction in the treatment. Interference between Pe and NN has very decisive role in forming the shape of FDCS, especially at large η values.

Interestingly, large discrepancies can also be observed among theories in predicting the contribution for the Pe at $\eta = 1.38$ (not presented in the figures): intensive single peaks (the magnitude three to five times higher than the measured one) at $\theta_e = 0°$ are presented in the CDW-EISPI, CCW-PT calculations, while in 3C the peak is in the order of magnitude of the experiment and in MCB-PI a deep is predicted. This fact together with the various treatments on NN explains the large discrepancies among the theoretical data.

The vertical dotted lines in Fig. 5 denote predicted positions of the binary (BP) ($\theta_e \geqslant 0°$) and shifted recoil peaks (SRP) ($\theta_e \leqslant 0°$), respectively [12]. It is well seen that there is a shift between the predicted and measured positions of the BP peak, and no peak is predicted at the position of SRP. In Refs. [12,13] the shift was attributed to a projectile as penetrating or passing out the electron cloud of the target atom, respectively. Such a picture cannot be justified in the present description, where the projectile is found passing by the target most likely from outside of the electron cloud.

4. Description of the passive electron

The present results, in agreement with the conclusion found in Ref. [16], that both the correlated motion of the ionized electron and the NN interaction can take a relatively important role in the description of the collision process, also point out the importance of the correct description of the passive electron. The role of the passive electron is considered in two aspects in our treatment. (i) Description of the unperturbed atomic orbitals in both the initial and the final channels. The present CDW-EIS application and calculation found in Ref. [13] differ mostly in accounting for the screening effect of passive electron. In Ref. [13], for both the Pe and the NN mechanisms, the role of the nonactive electron is taken into account by a constant effective charge. In the present treatment the unperturbed atomic orbitals are evaluated on a more realistic Hartree-Fock-Slater potential, and so the orthogonality of the initial and final unperturbed atomic wave functions is also satisfied. These differences in the two CDW-EIS treatments are mostly reflected in the absolute magnitude of the FDCS, the shape is hardly affected. (ii) The other area where screening of the passive electron is taken into account is the interaction between the projectile and the target core. In our treatment the static screening is considered by $V_s(R)$ of Eq. (5) and, in addition, polarization effect on the nonactive electron by the incoming projectile has also be taken into account. As the static screening plays a role mostly in distances where $V_s(R)$ already takes it asymptotic limits the present CDW-EIS and of Ref. [13] predict similar FDCS results (see Fig. 5 and 6). However, taking into account the polarization in the treatment the FDCS is changed not only on the absolute scale but in its shape too. This effect is dramatic at large η values and show a possible way for the extension strategy of theoretical methods. Note that the important role of polarization was also identified in the ionization of Li by 1.5 MeV/amu O^{8+} impact [29].

Finally, we note that coherence properties of the projectile beam was not controlled in the experiment of Schulz *et al.* [12]. However, we performed calculations with coherence parameters smaller and larger than that applied in Ref. [23]. Changes in absolute magnitudes for all η and modifications in shapes at $\eta = 1.38$ were observed in the evaluated FDCSs. However, these variations do not fit a coherent picture that gives a better account and interpretation for the measurement of Ref. [12].

B. Collision with incoherent projectile beam

Recently Arthanayaka *et al.* [23] investigated the projectile coherence effects in single ionization of He by 75-keV H^+ projectile impact. FDCSs were measured at $\varepsilon = 30$ eV projectile energy loss, where the transverse coherent properties of the projectile beam was controlled by setting $d_x = 1.0$ or 3.5, while d_y was fixed to 3.5, see Eq. (12). FDCSs obtained with small and large d_x are referred to as incoherent and coherent cross sections, respectively. In the experiment $\mathbf{k}_f$ and $\mathbf{q}_{\text{rec}}$ were measured and the electron momentum was deduced from the momentum conservation $\mathbf{k}_e = \mathbf{q} - \mathbf{q}_{\text{rec}}$. The temperature of the target was $T \approx 1–2$ K, therefore, to a good approximation the initial momentum of the target beam is $\kappa \approx 0$. Velocity spread of the He gas beam and so the target
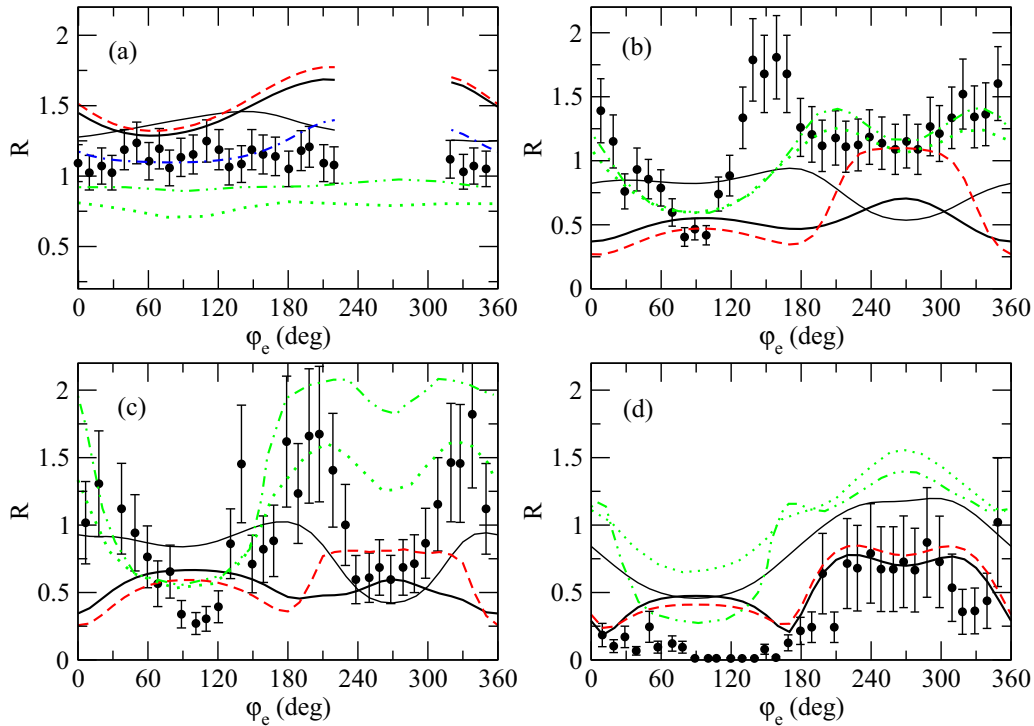
FIG. 7. Ratios of the FDCS for coherent and incoherent beams for $p_{recx} = 0.2$ a.u. and $\theta_e = 25°$ [panel (a)]; $p_{recx} = 0.7$ a.u. and $\theta_e = 45°$ [panel (b)]; $p_{recx} = 0.7$ a.u. and $\theta_e = 65°$ [panel (c)], and $q_{recx} = 1.25$ a.u. and $\theta_e = 65°$ [panel (d)]. Present results: with $(d_x, d_y) = (1.0, 3.5)$ a.u.; thin black lines: no NN interaction, heavy black lines: NN interaction with phase δ_3, dashed red lines: NN interaction with phase δ_4. Dotted and dot dot dashed green lines are perturbative and *ab initio* models from Ref. [23]. Experiment: • from [23]. In panel (a) the dot dashed blue line: present results with $(d_x, d_y) = (2.0, 7.0)$ a.u. and with NN taken by phase δ_3.

coherence was investigated by Kouzakov *et al.* [8] for the case of 100-MeV/amu C^{6+} He collision. The negligible role of the velocity spread for target was found at $T \approx 1–2$ K, however, evaluating the FDCS for the $T \approx 8–16$ K target temperature, good agreement with the experiment was reported. At the same time, Schulz *et al.* [42] argued that the experimental resolution is the main contributor to the discrepancy between experiment and theory, and concluded that the high temperature implied in Ref. [8] can be ruled out in the measurement. The measurement by Arthanayaka *et al.* [23] was performed at the same target temperature as the 100-MeV/amu C^{6+} He experiment, therefore, and expecting similar effects for the velocity spread the He beam, we neglected the role of target coherence and did not include the wave packet for the target in our treatment, see Eq. (10).

1. Coherent and incoherent ratios at fixed recoil ion momentum

In Fig. 7 the ratio R between the coherent and incoherent FDCS of Eq. (11) as a function of φ_e for $p_{recx} = 0.2$ and $\theta_e = 25°$, $p_{recx} = 0.7$ and $\theta_e = 45°$, $p_{recx} = 0.7$ and $\theta_e = 65°$ and $p_{recx} = 1.25$ and $\theta_e = 65°$ are presented. p_{recx} is the x component of the momentum of the recoiled ion, and $\mathbf{k}_e$ is deduced form the momentum conservation $\mathbf{k}_e = \mathbf{q} - \mathbf{q}_{rec}$. Note that $\mathbf{k}_e$ was not fixed in the measurement, however, its value was controlled by the experimental resolutions over which the evaluated FDCS was convolved. In atomic collision R is expected to reflect the interference between the different collisions mechanisms. Let us consider a simple single-center

interference phenomena where only two processes are included. It is supposed that the processes are characterized by transition probabilities dominated at ρ_1 and ρ_2 impact parameters. Then if $|\rho_1 - \rho_2|$ is less than d_x these two processes provides the coherent, otherwise the incoherent FDCS. In Ref. [23], the measured value of R ≈ 1 for $p_{recx} = 0.2$, indicates that the projectile beam characterized by $d_x = 1.0$ transverse coherence length, excites the target coherently [see Fig. 7(a)]. Structures, oscillations with φ_e at around $R = 1$ were observed for $p_{recx} = 0.7$, while for $p_{recx} = 1.25$ a drastic change, $R \approx 0$ values were recorded in the $0° \leqslant \varphi_e \leqslant 180°$ region. The coordinate system, in Ref. [23], was defined so that the x axis was fixed by the direction of $-\boldsymbol{\eta}$ [$\boldsymbol{\eta} = (\eta_x, 0)$] and φ_e is measured form the positive y axis. That is $\eta = p_{recx} + k_\perp \sin(\varphi_e)$ and η takes its lowest values (η_{min}) when $\varphi_e \geqslant 180°$. $\eta_{min} \approx 0$ for $p_{recx} = 0.2$ and $\theta_e = 25°$ and $\eta_{min} \approx 0.65$ for $p_{recx} = 1.25$ and $\theta_e = 65°$.

Our results for the ratios of the effective FDCSs of Eq. (11) are also presented in Fig. 7. Values of R are evaluated when the NN interaction is omitted (δ_0) or taken into account by phases δ_i with $i = 3$ and 4. Considerable discrepancies can be observed between results with and without the NN interaction for all p_{recx}. Reasonable agreements between our results and the experiment can be observed at $p_{recx} = 0.2$ and 1.25. First, let us discuss the result at $p_{recx} = 0.2$, where the measured $R \approx 1$ value indicates that the projectile excites the target similarly both in the coherence and the incoherence arrangements. At the same time our calculations, obtained with $(d_x, d_y) = (1.0, 3.5)$ coherence parameters, predict $R > 1$

for $\varphi_e \geqslant 120°$, and indicate the role of the single-center interference. Note that the region $220° \leqslant \varphi_e \leqslant 320°$ is excluded due to kinematical reasons. As it is discussed above, the Pe and NN processes give their dominant contributions to the FDCS in partly different ranges of the impact parameter space when η is small, and this separation (ρ_s) is characterized by $\rho_s \geqslant 1$ value. Therefore, the values of $R \neq 1$ is a clear signature of the interference in our treatment. That is the coherent and incoherent projectile beams activate differently the collisions processes. By increasing the coherence parameters, it is feasible that the incoherent beam excites the target coherently. Really, performing the calculation with d_x that $d_x \geqslant \rho_s$, like $(d_x, d_y) = (2.0, 7.0)$, we get the $R \approx 1$ result, and a reasonable account of the experiment is observed, see the dot dashed blue line in Fig. 7(a). It should be noted that in this calculation the coherent FDCS was derived directly from Eq. (3). In the other investigated cases, see Figs. 7(b) and 7(d), $\eta_{\min} \gg 0$, and for large η values, as found above, the interference between Pe and NN become important which can be constructive and destructive. Moreover, if one consider that the $\varphi_e \leqslant 180°$ region is represented by much larger η values than that of $\varphi_e \geqslant 180°$, various interference characters are reflected in values of R. This is why R takes very different values in the low and high φ_e regions, see Fig. 7(d).

In Figs. 7(b) and 7(c) the present results are in disagreement with the experiment especially when the NN interaction is included. Similar results, and so similar disagreements with the experiment, can be found in the application of the B1 approximation. Minimums or valleys in the FDCS discussed above do not present or much less pronounced in results of the B1 calculation when the NN interaction is included. Therefore, disagreements between theories and experiment cannot be related only to these structures. Indeed, values of R shown in Figs. 7(b) and 7(c), are evaluated in regions of FDCS which are less affected by dips and valleys. At medium and large η values, as found above, transition ranges of the Pe and NN processes are very broad, therefore, their interference might not be limited to a small region of ρ as for the case small η values. This is supported by the fact that the $R \approx 1$ values can only be reproduced in calculations with coherence length much larger ($d_x \geqslant 10$) than that fixed in the experiment.

In Fig. 7 results of perturbative and *ab initio* calculations from Ref. [23] are also presented. These models reproduce the basic features seen in the experimental data and provide better account of the experiment than the present one at $p_{recx} = 0.7$. In Ref. [23], see also Ref. [43], the ionization amplitude versus $\boldsymbol{\rho}$ is evaluated in a first Born and in an *ab initio* methods. In the later method the two-electron time-dependent Schrödinger equation is solved numerically. The wave packet associated with the projectile beam is described in coordinate space, where the time dependence and so the dispersion of the wave packet is neglected. Furthermore, each impact parameter was assigned with certain projectile scattering angle on the basis of classical scattering, that is, one-to-one correspondence between $\boldsymbol{\rho}$ and $\boldsymbol{\eta}$ was supposed. Based on these approximations and results for R(φ_e), Arthanayaka *et al.* [23] attributed a lesser role for the single center-interference and for the higher-order effects than that was discussed for the FDCS [12]. Instead, it was concluded that the observed variation of R (the interference) was due to the coherent superposition of
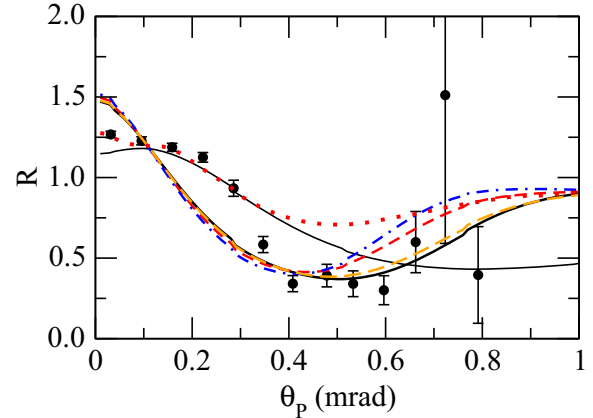

FIG. 8. Ratios between double differential cross sections measured for coherent and incoherent beams as a function of scattering angle of projectile. Present results with $(d_x, d_y) = (1.0, 3.5)$ a.u.; dashed black lines represent calculations without NN interaction: calculations where the NN interaction is represented by internuclear phase δ_i, $i = 2$–6 are denoted as thin solid black, heavy solid black, dotted red, long dashed turquoise, and dot dot dashed orange lines. Experiment: ● from Ref. [23].

different impact parameters resulting in the same scattering angle. This is known as path interference, see Ref. [44], which is supposed to be responsible for the observed interference in $R(\varphi_e)$ even in a first-order treatment.

Results and conclusions of Arthanayaka *et al.* [23] motivated us for the following comments, which also outline differences between their and our treatments. (i) Interference between the Pe and NN collision mechanism plays an important role in our interpretation. Therefore, we found essential to include contributions for the higher-order mechanisms even for a qualitative account for the measurement. Coherent superposition of processes, regardless of NN, is included or not, at the same impact parameter is also relevant. (ii) Our calculation revealed that a given $\boldsymbol{\eta}$ cannot be related to a given $\boldsymbol{\rho}$. We must also note that in our treatment coherent superposition of different impact parameter was considered in both coherent and incoherent calculations, and calculations with large coherence length provided the coherent FDCS. (iii) It should also be noted that the FDCS applied in Arthanayaka *et al.* [23,43]

$$\frac{d\sigma}{dE_e \Omega_{k_e} d\boldsymbol{\eta}} = \rho P(\rho) \left| \frac{d\rho}{d\eta} \right|, \quad (15)$$

where $P(\rho)$ is the ionization probability, was also derived and discussed in Refs. [45,46]. It was concluded that this formula is not very accurate, especially for low projectile scattering.

2. Coherent and incoherent ratios versus projectile scattering

In Fig. 8, ratios between double differential cross sections (DDCS) measured for coherent and incoherent projectile beams are plotted as a function of scattering angle for the projectile ion. The DDCS is obtained by integrating the FDCS of Eq. (11) over the emission angle of the electron. As it is expected, fine details observed in the FDCS are blurred in the DDCS, however, the role of NN is still important.

The present result derived without the NN interaction shows good agreement with the experiment only in the $\theta_P \leqslant 0.8$ mrad region, where all calculations including NN predict a stronger decrease of R with the increase of θ_P. Low projectile scattering corresponds to small η values where the Pe and NN mechanisms interferes constructively and the FDCSs with NN decrease more rapidly with η than that without the NN interaction, see Fig. 4. Calculations with NN show good results with the measurement for $\theta_P \geqslant 0.4$ mrad, where the large experimental error bars do not allow a more through evaluation. Discrepancies can be observed between the measurement and our results with δ_i, $i = 2$–6 in the $\theta_P \approx 0.25$ mrad region. The result of the B1 calculation where the NN interactions is taken into account by δ_4 is also shown in the figure. This result presents nice agreement with the measured data for $\theta_P \leqslant 0.4$ mrad. Note the the B1 approximation without NN fails to reproduce the measurement in the whole angular range.

As Figs. (3) and (4) show dips and valleys are present in the FDCS at low and medium η values. These structures become less pronounced when the coherent FDCS is convolved with finite projectile coherence parameters. As a result, in some regions, the incoherent FDCS takes higher values than the coherent one and so R becomes lower than that which corresponds to the case with no minimums, like the one without NN. This is the reason why the CDW-EIS underestimate the experiment at $\theta_P \approx 0.25$ mrad. At the same time, if one consider results of B1 and CDW-EIS approximations, it can be concluded that the NN interaction has a significant role in the whole angular range, and that higher-order effects are unimportant at the low projectile scattering. We also note that taking $d_x = 3.5$ in the evaluation, the incoherent DDCS is identical to the coherent one.

IV. SUMMARY AND CONCLUSION

In this paper we apply the continuum distorted wave with eikonal initial state approximation to describe ionization of He under the impact of 75-keV H^+ ion. Fully differential cross sections are evaluated within the framework of the independent electron approximation. The role of the internuclear interaction (NN) is taken into account by a phase factor, and projectile coherence properties considered in a wave-packet description.

Coulomb interaction of the heavy nuclei, screening of the passive electron, and the polarization of the target core by the incident projectile ion are included in the NN interaction term. V_{pol} is not uniquely defined for short distances and accordingly different approaches and different forms of V_{pol} are applied in the treatment. FDCS has been analyzed in both the scattering and the perpendicular plane. The importance of the NN interaction is assessed for almost all the studied studied regions of the FDCS. It is found that there is a qualitative agreement between our calculation and the measurement. The observed discrepancies and comparison of our results to other theoretical calculations show that the evaluated cross sections are very sensitive to the details on the description of the interaction between the projectile and the target core. The strong influence of V_{pol} on the evaluated FDCS is observed for large η values. The complexity of NN interactions is further emphasized if one consider the lowest η

region where calculations with no NN reveal better accounts with the experiment.

Our calculations predict minimums and valley-like structures in the FDCS at some combinations of $\boldsymbol{\eta}$ and $\mathbf{k}_e$, which are more obvious when the NN interaction is included in the treatments. Dips are well observable when the FDCSs are plotted versus η. The available experimental data do not fully justify the reality of these structures as different aspects were considered in selecting the kinematic parameters in the measurements. However, we think that at medium and large η values a realistic FDCS has considerable areas where its value changes rapidly with $\mathbf{k}_q$ or $\boldsymbol{\eta}$. The variability of the FDCS is strongly affected by V_{pol}, which should be considered in subsequent applications.

As it is shown, there are cases where all of the discussed theories are unable to describe the FDCS, see, e.g., results of panels (c) and (d) in Figs. 1 and 2. Therefore, we convolved the FDCS derived for NN phase of δ_6 with the experimental uncertainties, which are presented as thin lines with triangle up in Figs. 1 and 2. As it is seen, taking into account experimental uncertainties does not improve considerably the agreement between theory and experiment. We might also refer to the case of 100-MeV/amu C^{6+}-He collision, where the inclusion of experimental uncertainties in the treatment can only explain part of the discrepancies [42,47]. We also evaluated FDCS with different coherence parameters and compared to the experiment. Improved agreements were obtained only for some cases, and no definite conclusion can be drawn. Further studies on the experimental side would also be helpful, like investigating coherent and incoherent FDCSs of Ref. [23] as given in Sec. III A.

Incoherent properties of the projectile beam is considered by taking ratios of coherent and incoherent FDCS values. Our calculations reveal the importance of the NN interaction for all the studied p_{recx} values. At $p_{recx} = 0.2$ the role of interference between Pe and NN mechanisms has been observed. At the $p_{recx} = 0.7$ the present results is in disagreement with the measurement due to the mentioned minimums in the FDCS evaluated with inclusion of the NN interaction. While for $p_{recx} = 1.25$ our results show a nice account with the experiment and show less sensitivity to details of the NN interaction.

Roles of singe-center interference were identified both in the coherent FDCSs and in the ratios of coherent and incoherent FDCSs. At small η values our results, in agreement with the other theoretical applications, overestimate the measurement that we explained by the constructive interference between the Pe and NN mechanisms. For the case of coherent and incoherent FDCS ratios, the measured $R \approx 1$ value at $p_{recx} = 0.2$ is reproduced in our calculation, when the transverse coherence length of the projectile beam (d_x) was increased so that it becomes larger than the separation between typical impact parameters of the Pe and NN processes.

APPENDIX A: FDCS

An evaluation of cross sections including initial wave packets for the projectile (Φ_p) and the target (Φ_t). Let us consider a process, where a projectile ion (p) with momentum $\mathbf{K}$ and energy E_p collides with a target (t) having momentum $\boldsymbol{\kappa}$ and translation energy E_t. After the collision one electron (e) with momentum $\mathbf{k}_e$ and energy E_e is released, while the projectile and the recoiled ion leave the collision zone, respectively, with $\mathbf{K}'$ and $\boldsymbol{\kappa}'$ momenta and E_p and $E_{\rm ion}$ energies:

$$\mathrm{p}\,(\mathbf{K}, \mathrm{E_p}) + \mathrm{t}\,(\boldsymbol{\kappa}, \mathrm{E_t} \sim 0) \rightarrow \mathrm{p}\,(\mathbf{K}', \mathrm{E_p'}) + \mathrm{ion}\,(\boldsymbol{\kappa}', \mathrm{E_{ion}} \sim 0) + \mathrm{e}\,(\mathbf{k_e}, \mathrm{E_e}),$$

$$E_p = \frac{K^2}{2M_p}, \quad E_p' = \frac{K'^2}{2M_p}, \quad E_t = \frac{\kappa^2}{2M_t}, \quad E_{\rm ion} = \frac{\kappa'^2}{2(M_t - 1)}, \quad E_e = \frac{k_e^2}{2}, \tag{A1}$$

where and M_p and M_t are the mass of projectile ion and target atom. The FDCS is written as [41,48,49]

$$\frac{d\sigma}{d\mathbf{k}_e d\boldsymbol{\kappa}' d\mathbf{K}'} = \int d\mathbf{K} |\Phi_p(\mathbf{K})|^2 \int d\boldsymbol{\kappa} |\Phi_t(\boldsymbol{\kappa})|^2 \frac{|T_{fi}|^2}{(2\pi)^2 v_\parallel} \delta(\mathbf{K}' + \mathbf{k}_e + \boldsymbol{\kappa}' - \mathbf{K} - \boldsymbol{\kappa})\,\delta(E_p' + E_e + I - E_p), \tag{A2}$$

where T_{fi} denotes the T matrix, I is the ionization energy, and kinetic energies of the target atom and target ion are neglected in the δ function. Note that $\mathcal{R}$ in our formulation relates to T by $\lim_{\mu \to \infty} |\mathcal{R}(\boldsymbol{\eta})_{i\mathbf{k}}| = |1/v T_{if}(\eta/\mu/v)|$ [31]. $|\Phi_p(\mathbf{K})|^2$ and $|\Phi_t(\boldsymbol{\kappa})|^2$ are peaked at $\mathbf{K} = \mathbf{K}_0 = (0, 0, K_0)$ and $\boldsymbol{\kappa} = \mathbf{0}$, respectively, and they are normalized by $\int |\Phi_{p,t}(\mathbf{p})|^2 d\mathbf{p} = 1$. We define $\mathbf{v} = \mathbf{K}/M_p$ and $\mathbf{v}_0 = \mathbf{K}_0/M_p$, and $v_\parallel = K_z/M_p$, and in the following different presentations of the FDCS are considered.

1. When $\mathbf{k}_e$ and $\mathbf{K}'$ are selected

The DCS is obtained by integrating Eq. (A2) over $\boldsymbol{\kappa}'$ as

$$\frac{d\sigma}{d\mathbf{k}_e d\mathbf{K}'} = \int d\mathbf{K} |\Phi_p(\mathbf{K})|^2 \int d\boldsymbol{\kappa} |\Phi_t(\boldsymbol{\kappa})|^2 \frac{|T_{fi}|^2}{(2\pi)^2 v_\parallel} \delta(E_p' + E_e + I - E_p), \tag{A3}$$

with $\boldsymbol{\kappa}' = \mathbf{K} - \mathbf{K}' + \boldsymbol{\kappa} - \mathbf{k}_e$. To see the form of the T matrix, let us consider T_{fi} in the Born approximation

$$T_{fi}^{B1}(\mathbf{k}' \leftarrow \mathbf{k}) = \langle e^{i\mathbf{k}'\mathbf{R}} \phi_{\mathbf{k}_e} | V_i | e^{i\mathbf{k}\mathbf{R}} \phi_i \rangle \tag{A4}$$

with

$$\mathbf{k} = (M_t \mathbf{K} - M_p \boldsymbol{\kappa})/(M_p + M_t),$$
$$\mathbf{k}' = (M_t \mathbf{K}' - M_p[\mathbf{k}_e + \boldsymbol{\kappa}'])/(M_p + M_t), \quad \langle \phi_{\mathbf{k}_e} | \phi_{\mathbf{k}_e'} \rangle = \delta(\mathbf{k}_e - \mathbf{k}_e'), \tag{A5}$$

where $\mathbf{k}$ and $\mathbf{k}'$ are the relative momenta in the center-of-mass system and $\mathbf{R}$ is the relative coordinate of the projectile from the target. Note that $\mathbf{k} - \mathbf{k}' = \{M_t(\mathbf{K} - \mathbf{K}') + M_p(\boldsymbol{\kappa}' + \mathbf{k}_e - \boldsymbol{\kappa}_t)\}/(M_p + M_t) = \mathbf{K} - \mathbf{K}'$ by the momentum conservation.

Integrating over K_z using the energy conservation, Eq. (A3) becomes

$$\frac{d\sigma}{d\mathbf{k}_e d\mathbf{K}'} = M_p/K_z \int d\mathbf{K}_\perp |\Phi_p(\mathbf{K})|^2 \int d\boldsymbol{\kappa} |\Phi_t(\boldsymbol{\kappa})|^2 \frac{|T_{fi}|^2}{(2\pi)^2 v_\parallel},$$
$$= \int d\mathbf{K}_\perp |\Phi_p(\mathbf{K})|^2 \int d\boldsymbol{\kappa} |\Phi_t(\boldsymbol{\kappa})|^2 \frac{|T_{fi}|^2}{(2\pi v_\parallel)^2}, \tag{A6}$$

with $K_z = \sqrt{K'^2 - K_\perp^2 + 2M_p(E_e + I)}$.

From now on, we assume that $|\mathbf{v} - \mathbf{v}_0| \ll v_0$, $|\boldsymbol{\kappa}/M_t| \ll v_0$, and that the T matrix is a function of $\mathbf{Q}_\perp = (\mathbf{K} - \mathbf{K}')_\perp$ and $\mathbf{v}_0$ as usual in the semiclassical collision theory. With change of variables $\mathbf{K}_\perp \to \mathbf{Q}_\perp = \mathbf{K}_\perp - \mathbf{K}'_\perp$, Eq. (A6) is reduced to

$$\frac{d\sigma}{d\mathbf{k}_e d\mathbf{K}'} \simeq \int d\mathbf{Q}_\perp |\Phi_p(\mathbf{K})|^2 \int d\boldsymbol{\kappa} |\Phi_t(\boldsymbol{\kappa})|^2 \frac{|T_{fi}(\mathbf{Q}_\perp, \mathbf{v}_0)|^2}{(2\pi v_0)^2}$$
$$\simeq \int d\mathbf{Q}_\perp |\Phi_p(\mathbf{K})|^2 \frac{|T_{fi}(\mathbf{Q}_\perp, \mathbf{v}_0)|^2}{(2\pi v_0)^2}, \tag{A7}$$

with $K_z \simeq K_z' + M_p(E_e + I)/K_z' \simeq K_z' + Q_z$ and $Q_z = (E_e + I)/v_0$. In the above equation the integration over $\boldsymbol{\kappa}$ is separable, and $\int d\boldsymbol{\kappa} |\Phi_t(\boldsymbol{\kappa})|^2 = 1$ is used. When $\Phi_p(\mathbf{K})$ is written as $\Phi_p^\perp(\mathbf{K}_\perp) \times \Phi_p^\parallel(K_z)$, Eq. (A7) becomes

$$\frac{d\sigma}{d\mathbf{k}_e d\mathbf{K}'} \simeq |\Phi_p^\parallel(K_z)|^2 \int d\mathbf{Q}_\perp |\Phi_p^\perp(\mathbf{K}_\perp = \mathbf{Q}_\perp + \mathbf{K}'_\perp)|^2 \frac{|T_{fi}(\mathbf{Q}_\perp, \mathbf{v}_0)|^2}{(2\pi v_0)^2}. \tag{A8}$$

Integrating by K_z', we have

$$\frac{d\sigma}{d\mathbf{k}_e d\mathbf{K}_\perp'} \simeq C_1 \int d\mathbf{Q}_\perp |\Phi_p^\perp(\mathbf{Q}_\perp - \mathbf{q}_\perp)|^2 \frac{|T_{fi}(\mathbf{Q}_\perp, \mathbf{v}_0)|^2}{(2\pi v_0)^2}, \tag{A9}$$

with $C_1 = \int |\Phi_p^\parallel(K_z' + Q_z)|^2 dK_z'$ and $\mathbf{q}_\perp = (\mathbf{K}_0)_\perp - \mathbf{K}_\perp'$.

2. When κ' and $\mathbf{K}'$ are selected

The DCS is obtained by integrating Eq. (A2) over $\mathbf{k}_e$ as

$$\frac{d\sigma}{d\kappa' d\mathbf{K}'} = \int d\mathbf{K} |\Phi_p(\mathbf{K})|^2 \int d\kappa_t |\Phi_t(\kappa)|^2 \frac{|T_{fi}|^2}{(2\pi)^2 v_\parallel} \delta(E_p' + E_e + I - E_p), \tag{A10}$$

with $\mathbf{k}_e = \mathbf{K} - \mathbf{K}' + \kappa - \kappa'$. Similarly to Eq. (A6), we have

$$\frac{d\sigma}{d\kappa' d\mathbf{K}'} = \int d\mathbf{K}_\perp |\Phi_p(\mathbf{K})|^2 \int d\kappa |\Phi_t(\kappa)|^2 \frac{|T_{fi}|^2}{(2\pi v_\parallel)^2} \tag{A11}$$

with $K_z \simeq K_z' + Q_z$ and $Q_z = (E_e + I)/v_0$. Applying the semiclassical condition, the above equation becomes

$$\frac{d\sigma}{d\kappa' d\mathbf{K}'} = \int d\mathbf{K}_\perp |\Phi_p(\mathbf{K})|^2 \int d\kappa |\Phi_t(\kappa)|^2 \frac{|T_{fi}(\mathbf{Q}_\perp, \mathbf{v}_0)|^2}{(2\pi v_0)^2}. \tag{A12}$$

With change of variables $\{\mathbf{K}_\perp, \kappa\} \to \{\mathbf{Q}_\perp = \mathbf{K}_\perp - \mathbf{K}_\perp', \mathbf{k}_e\}$, we have

$$\frac{d\sigma}{d\kappa' d\mathbf{K}'} = \int d\mathbf{k}_e \int d\mathbf{Q}_\perp |\Phi_p(\mathbf{K})|^2 |\Phi_t(\kappa)|^2 \frac{|T_{fi}(\mathbf{Q}_\perp, \mathbf{v}_0)|^2}{(2\pi v_0)^2}, \tag{A13}$$

with $\mathbf{K} = \mathbf{Q} + \mathbf{K}'$ and $\kappa = \kappa' + \mathbf{k}_e - \mathbf{Q}$.

Assuming that $\Phi_{p,t}(\mathbf{p}) = \Phi_{p,t}^\perp(\mathbf{p}_\perp) \times \Phi_{p,t}^\parallel(p_z)$, we have

$$\frac{d\sigma}{d\kappa' d\mathbf{K}_\perp'} = |\Phi_p^\parallel(K_z' + Q_z)|^2 \int d\mathbf{k}_e |\Phi_t^\parallel(\kappa_z)|^2 \int d\mathbf{Q}_\perp |\Phi_p^\perp(\mathbf{K}_\perp)|^2 |\Phi_t^\perp(\kappa_\perp)|^2 \frac{|T_{fi}(\mathbf{Q}_\perp, \mathbf{v}_0)|^2}{(2\pi v_0)^2}, \tag{A14}$$

with $\kappa_z = \kappa_z' + (k_e)_z - Q_z$. Integrating the above equation over K_z' gives

$$\frac{d\sigma}{d\kappa' d\mathbf{K}_\perp'} = C_2 \int d\mathbf{k}_e |\Phi_t^\parallel(\kappa_z)|^2 \int d\mathbf{Q}_\perp |\Phi_p^\perp(\mathbf{K}_\perp)|^2 |\Phi_t^\perp(\kappa_\perp)|^2 \frac{|T_{fi}(\mathbf{Q}_\perp, \mathbf{v}_0)|^2}{(2\pi v_0)^2}, \tag{A15}$$

with $C_2 = \int |\Phi_p^\parallel(K_z' + Q_z)|^2 dK_z'$.

3. When $\mathbf{k}_e$ and κ' are selected

The DCS is obtained by integrating Eq. (A2) over $\mathbf{K}'$ as

$$\frac{d\sigma}{d\mathbf{k}_e d\kappa'} = \int d\mathbf{K} |\Phi_p(\mathbf{K})|^2 \int d\kappa |\Phi_t(\kappa)|^2 \frac{|T_{fi}|^2}{(2\pi)^2 v_\parallel} \delta(E_p' + E_e + I - E_p), \tag{A16}$$

with $\mathbf{K}' = \mathbf{K} + \kappa - \mathbf{k}_e - \kappa'$. By change of variables $\{\mathbf{K}, \kappa\} \to \{\mathbf{K}, \mathbf{Q} = \mathbf{K} - \mathbf{K}'\}$, the above equation becomes

$$\frac{d\sigma}{d\mathbf{k}_e d\kappa'} = \int d\mathbf{K} |\Phi_p(\mathbf{K})|^2 \int d\mathbf{Q} |\Phi_t(\kappa)|^2 \frac{|T_{fi}|^2}{(2\pi)^2 v_\parallel} \delta(E_p' + E_e + I - E_p), \tag{A17}$$

with $\kappa = \mathbf{k}_e + \kappa' - \mathbf{Q}$. Approximating $E_p' + E_e + I - E_p = 0$ by $\{(\mathbf{K} - \mathbf{Q})^2 - K^2\}/(2M_p) + E_e + I \simeq -\mathbf{v}_0\mathbf{Q} + E_e + I = 0$, we have

$$\frac{d\sigma}{d\mathbf{k}_e d\kappa'} = \int d\mathbf{K} |\Phi_p(\mathbf{K})|^2 \times \int d\mathbf{Q}_\perp |\Phi_t(\mathbf{k}_e + \kappa' - \mathbf{Q})|^2 \frac{|T_{fi}(\mathbf{Q}_\perp, \mathbf{v}_0)|^2}{(2\pi v_0)^2}$$

$$= \int d\mathbf{Q}_\perp |\Phi_t(\mathbf{k}_e + \kappa' - \mathbf{Q})|^2 \frac{|T_{fi}(\mathbf{Q}_\perp, \mathbf{v}_0)|^2}{(2\pi v_0)^2}, \tag{A18}$$

with $Q_z = (E_e + I)/v_0$. When $\Phi_t(\kappa)$ is written as a product $\Phi_t^\perp(\kappa_\perp) \times \Phi_t^\parallel(\kappa_z)$, the above equation becomes

$$\frac{d\sigma}{d\mathbf{k}_e d\kappa'} = |\Phi_t^\parallel(k_{e,z} + \kappa_z' - Q_z)|^2 \int d\mathbf{Q}_\perp |\Phi_t^\perp(\kappa_\perp)|^2 \frac{|T_{fi}(\mathbf{Q}_\perp, \mathbf{v}_0)|^2}{(2\pi v_0)^2}. \tag{A19}$$

APPENDIX B: B1 APPROXIMATION

The square of the transition amplitude for ionization of an electron in the first Born approximation is given as [31]

$$|T^{B1}|^2 = \frac{2^{12}\pi^3 Z_P Z_{\text{eff}}^5 |N(k_e)|^2 A}{q^2 \left[(Z_{\text{eff}} + q^2 - k_e^2)^2 + 4Z_{\text{eff}}^2 k_e^2 \right] T^4} \exp\left\{ \frac{2Z_{\text{eff}}}{k_e} \tan^{-1} \frac{2Z_{\text{eff}} k_e}{Z_{\text{eff}}^2 - k_e^2 + q^2} \right\}, \tag{B1}$$

where

$$T = Z_{\text{eff}}^2 + k_e^2 + q^2 - 2\mathbf{k}_e \mathbf{q}, \tag{B2}$$

and

$$A = \left(q - \frac{\mathbf{k}_e \mathbf{q}}{q} \right)^2 + Z_{\text{eff}}^2 \left(\frac{\mathbf{k}_e \mathbf{q}}{k_e q} \right)^2. \tag{B3}$$

Z_{eff} is the nuclear charge of the target.

[1] J. Ullrich, R. Moshammer, A. Dorn, R. Dörner, L. P. H. Schmidt, and H. Schmidt-Böcking, Rep. Prog. Phys. **66**, 1463 (2003).

[2] M. Schulz, D. Fischer, R. Moshammer, and J. Ullrich, J. Phys. B: At. Mol. Opt. Phys. **38**, 1363 (2005).

[3] M. Schulz, M. F. Ciappina, T. Kirchner, D. Fischer, R. Moshammer, and J. Ullrich, Phys. Rev. A **79**, 042708 (2009).

[4] M. S. Schöffler, J. N. Titze, L. P. H. Schmidt, T. Jahnke, O. Jagutzki, H. Schmidt-Böcking, and R. Dörner, Phys. Rev. A **80**, 042702 (2009).

[5] M. Schulz, *Advances In Atomic, Molecular, and Optical Physics* (Academic, New York, 2017), Vol. 66, pp. 507–543.

[6] M. Schulz *et al.*, J. Phys. B: At. Mol. Opt. Phys. **34**, L305 (2001).

[7] J. Fiol, S. Otranto, and R. E. Olson, J. Phys. B: At. Mol. Opt. Phys. **39**, L285 (2006).

[8] K. A. Kouzakov, S. A. Zaytsev, Y. V. Popov, and M. Takahashi, Phys. Rev. A **86**, 032710 (2012).

[9] M. Schulz, R. Moshammer, D. Fischer, and J. Ullrich, J. Phys. B: At. Mol. Opt. Phys. **36**, L311 (2003).

[10] K. N. Egodapitiya, S. Sharma, A. Hasan, A. C. Laforge, D. H. Madison, R. Moshammer, and M. Schulz, Phys. Rev. Lett. **106**, 153202 (2011).

[11] X. Wang, K. Schneider, A. LaForge, A. Kelkar, M. Grieser, R. Moshammer, J. Ullrich, M. Schulz, and D. Fischer, J. Phys. B: At. Mol. Opt. Phys. **45**, 211001 (2012).

[12] M. Schulz, A. Hasan, N. V. Maydanyuk, M. Foster, B. Tooke, and D. H. Madison, Phys. Rev. A **73**, 062704 (2006).

[13] M. F. Ciappina, W. R. Cravero, and M. Schulz, J. Phys. B: At., Mol. Opt. Phys. **40**, 2577 (2007).

[14] X. Y. Ma, X. Li, S. Y. Sun, and X. F. Jia, Euro. Phys. Lett. **98**, 53001 (2012).

[15] Y. H. Duan, S. Y. Sun, and X. F. Jia, Euro. Phys. Lett. **110**, 13001 (2015).

[16] X. Niu, S. Sun, F. Wang, and X. Jia, Phys. Rev. A **96**, 022703 (2017).

[17] J. M. Feagin and L. Hargreaves, Phys. Rev. A **88**, 032705 (2013).

[18] L. Sarkadi, I. Fabre, F. Navarrete, and R. O. Barrachina, Phys. Rev. A **93**, 032702 (2016).

[19] K. Schneider, M. Schulz, X. Wang, A. Kelkar, M. Grieser, C. Krantz, J. Ullrich, R. Moshammer, and D. Fischer, Phys. Rev. Lett. **110**, 113201 (2013).

[20] T. P. Arthanayaka, S. Sharma, B. R. Lamichhane, A. Hasan, J. Remolina, S. Gurung, and M. Schulz, J. Phys. B: At. Mol. Opt. Phys. **48**, 071001 (2015).

[21] L. Gulyás, P. D. Fainstein, and A. Salin, J. Phys. B **28**, 245 (1995).

[22] L. Gulyás, A. Igarashi, P. D. Fainstein, and T. Kirchner, J. Phys. B: At. Mol. Opt. Phys. **41**, 025202 (2008).

[23] T. Arthanayaka, B. R. Lamichhane, A. Hasan, S. Gurung, J. Remolina, S. Borbly, F. Jrai-Szab, L. Nagy, and M. Schulz, J. Phys. B: At., Mol. Opt. Phys. **49**, 13LT02 (2016).

[24] N. Stolterfoht, R. D. DuBois, and R. D. Rivarola, *Electron Emission in Heavy Ion-Atom Collisions* (Springer, Berlin, 1997).

[25] M. Foster, D. H. Madison, J. L. Peacher, M. Schulz, S. Jones, D. Fischer, R. Moshammer, and J. Ullrich, J. Phys. B: At. Mol. Opt. Phys. **37**, 1565 (2004).

[26] A. Igarashi and L. Gulys, J. Phys. B: At. Mol. Opt. Phys. **51**, 035201 (2018).

[27] C. J. Joachain, *Quantum Collision Theory* (North-Holland, Amsterdam, 1975).

[28] H. R. J. Walters and C. T. Whelan, Phys. Rev. A **89**, 032709 (2014).

[29] L. Gulyás, S. Egri, and T. Kirchner, Phys. Rev. A **90**, 062710 (2014).

[30] J. H. McGuire, *Electron Correlation Dynamics in Atomic Collisions* (Cambridge University Press, Cambridge, England, 1997).

[31] M. R. McDowell and J. P. Coleman, *Introduction to the Theory of Ion-Atom Collisions* (North-Holland, Amsterdam, 1970).

[32] D. S. F. Crothers and L. J. Dube, in *Advances in Atomic, Molecular, and Optical Physics*, edited by D. Bates and B. Bederson, (1992), Vol. 30, p. 287.

[33] P. D. Fainstein, L. Gulyás, and A. Salin, J. Phys. B: At. Mol. Opt. Phys. **29**, 1225 (1996).

[34] I. Y. Yurova and V. V. Kuverova, Russ. J. Phys. Chem. B **8**, 9 (2014).

[35] J. Mitroy, M. S. Safronova, and C. W. Clark, J. Phys. B: At. Mol. Opt. Phys. **43**, 202001 (2010).

[36] H. Nakanishi and D. M. Schrader, Phys. Rev. A **34**, 1810 (1986).

[37] D. M. Schrader, Phys. Rev. A **20**, 918 (1979).

[38] X. Zhang, J. Sun, and Y. Liu, J. Phys. B: At. Mol. Opt. Phys. **25**, 1893 (1992).

[39] C. Bottcher, J. Phys. B: At. Mol. Opt. Phys. **4**, 1140 (1971).

[40] D. V. Karlovets, G. L. Kotkin, and V. G. Serbo, Phys. Rev. A **92**, 052703 (2015).

[41] K. A. Kouzakov, Eur. Phys. J. D **71**, 63 (2017).

[42] M. Schulz, R. Moshammer, D. Fischer, and J. Ullrich, Phys. Rev. A **87**, 046701 (2013).

[43] F. Járai-Szabó and L. Nagy, Eur. Phys. J. D **69**, 4 (2015).

[44] L. Sarkadi, Phys. Rev. A **82**, 052710 (2010).

[45] B. H. Bransden and M. R. C. McDowell, *Charge Exchange and Thory of Ion-Atom Collisions* (Oxford Scientific, New York, 1995).

[46] P. T. Greenland, J. Phys. B: At., Mol. Opt. Phys. **14**, 3707 (1981).

[47] M. Dürr, B. Najjari, M. Schulz, A. Dorn, R. Moshammer, A. B. Voitkiv, and J. Ullrich, Phys. Rev. A **75**, 062708 (2007).

[48] J. R. Taylor, *Scattering Theory: The Quatum Theory of Nonrelativiscic Collisions* (Wiley, New York, 1972).

[49] C. J. Joachain, *Quantum Collision Theory* (North-Holland, Amsterdam, 1975).